Acoustic polygonal Bessel vortices based on metasurfaces

Yang Sun,[1] Wei-Xu Cao,[1] Xin-Rui Li,[1,2,*] Qi Wei,[1,†] Xing-Feng Zhu,[1] Jie Yao,[1] and Da-Jian Wu[1,‡]

[1] *Jiangsu Key Lab of Opto-Electronic Technology, School of Physics and Technology, Nanjing Normal University, Nanjing 210023, China*

[2] *Department of Architecture, College of Design and Environment, National University of Singapore, Singapore 117566, Singapore*

(Received 12 December 2023; revised 18 March 2024; accepted 29 March 2024; published 16 April 2024)

Acoustic vortices (AVs) play a significant role in the fields of acoustic communication and microparticle manipulation. Traditional AVs exhibit doughnut-shaped intensity profiles, which may restrict their application scenarios. Here, we propose an acoustic polygonal Bessel vortex (APBV), which can be generated by the coaxial coupling of multiple acoustic asymmetric Bessel vortices (AABVs). The number of sides of the APBV is dependent on the number of superimposed AABVs. Both topological charge and asymmetry coefficient of the AABV impact on the performance of the APBV, and the APBV also exhibits excellent nondiffracting characteristics. Moreover, an acoustic reflection metasurface (ARM) consisting of grooved units is designed to realize the APBV in air. Through simulations and experiments, we verify the generation of the APBV by the proposed ARM. The APBV may find potential applications in the polygonal manipulation of microparticles and acoustic communication.

DOI: 10.1103/PhysRevApplied.21.044029

I. INTRODUCTION

Acoustic vortices (AVs) carrying orbital angular momentum (OAM) have attracted a lot of scientific interest due to their unique applications in microparticle trapping and manipulation [1–4], and acoustic communication [5–11]. Over the past decade, various AVs have been investigated for a variety of applications [1–17]. The intensity profile of a standard AV with integer topological charge (TC) is radially symmetric and has a doughnut-shaped form. Many studies have been conducted on the use of the integer AVs to trap, levitate, manipulate, and rotate particles and living cells [1–4,12,13]. The fractional AV exhibits an extra radial phase discontinuity, which leads to a low-intensity gap on the annular intensity pattern. This additional factor facilitates the transit of microparticles and audio communication [14–17]. The propagation-invariant and nondiffraction properties of Bessel AVs make them ideal for long-distance transmission of information [18–21]. The asymmetry serves as a substitute factor to modify the acoustic OAM and enhance the singularity behavior of AVs. More recently, polygonal vortices have been explored in optics [22–32]. Kovalev and Kotlyar [24] reported a type of polygonal vortex that might alter the field distribution without altering the OAM. Xia *et al.* [31,32] developed polygonal vortices with tunable shapes, sizes, and TCs, which can trap particles along various polygonlike curves. It was reported that micromanipulation may be made simpler with a perfect polygonal optical vortex that has variable energy distribution at its vertices. Nevertheless, there has not yet been any reporting of the investigation on acoustic polygonal vortices. Acoustic polygonal vortices, if they could be realized, may be developed for acoustic communication and particle manipulation technologies, such as manipulating polygonal-shaped objects, collecting and/or trapping particles into polygonal regions, and moving particles along polygonal trajectories.

In this work, we realize an acoustic polygonal Bessel vortex (APBV) via the coaxial couplings between multiple acoustic asymmetric Bessel vortices (AABVs). The number of AABVs determines how many sides the APBV has. The propagation characteristics of APBVs as well as the acoustic intensity and phase distributions are investigated. We go into great detail into how the asymmetry parameter and TC of AABVs affect the acoustic characteristics of the APBV. Moreover, an acoustical reflective metasurface (ARM) composed of grooved structural units is designed to achieve the APBV in air. We also conduct experiments to verify that the suggested ARM realizes the APBV.

II. ACOUSTIC POLYGONAL BESSEL VORTEX

The APBV can be constructed by coupling several AABVs. In a cylindrical coordinate system, the complex

*Corresponding authors: e1320489@u.nus.edu
†weiqi@njnu.edu.cn
‡wudajian@njnu.edu.cn

amplitude of an AABV is expressed as follows [33]:

$$p_l(r,\theta,z) = \exp(il\theta)\exp(ik_r z)\sum_{q=0}^{\infty}\frac{\beta^q \exp(iq\theta)}{q!}J_{l+q}(k_z r), \tag{1}$$

where r, θ, and z represent the radial distance, the angular coordinate, and the axial coordinate of the cylindrical coordinate system; J_{l+q} is the $(l+q)$th-order Bessel function; l is the TC; q is the number of superimposed Bessel vortices; and k_z and k_r are the axial and radial wave vectors, respectively. The complex parameter $\beta = \beta_0\exp(i\varphi)$ is an asymmetry parameter, where the real part β_0 is the asymmetry index and can only regulate the asymmetry of AABV, while the imaginary part φ denotes the initial rotation angle of the AABV. Equation (1) can be further simplified to [34]

$$p_l(r,\theta,z) = \exp(il\theta)exp\,(ik_r z)\left[\frac{k_z r}{k_z r - 2\beta\exp(i\theta)}\right]^{l/2} J_l \left\{\sqrt{k_z r[k_z r - 2\beta\exp(i\theta)]}\right\}. \tag{2}$$

When $\beta_0 = 0$, Eq. (2) returns to the formula of a standard Bessel vortex.

In Figs. 1(a1)–1(a4), we plot the normalized theoretical acoustic intensity distributions of AABVs with the β_0 values of 0, 1, 4, and 7, respectively, according to Eq. (2). Here, $\varphi = 0$, $l = 2$, and the observation plane is at $z = 0$. Figures 1(b1)–1(b4) represent the corresponding phase profiles. As $\beta_0 = 0$, a distinct ring-shaped acoustic intensity distribution with a central null pressure is shown in Fig. 1(a1) and the phase shifts from $-\pi$ to π twice in an annular loop in a clockwise direction [in Fig. 1(b1)]. These properties are in accord with those of a Bessel vortex with $l = 2$. In Fig. 1(a2), for $\beta_0 = 1$, the acoustic intensity distribution changes to a crescent shape. Meanwhile, a phase singularity is observed at the center of Fig. 1(b2) and the phase still shifts from $-\pi$ to π twice. However, it can be clearly seen that, in addition to the central singularity, there are several new singularities appearing on the x axis that are paired, evenly numbered, and asymmetrically distributed on both sides of the origin. As β_0 increases to 4, the acoustic intensity distribution of the AABV changes to an arc-shaped pattern, as shown in Fig. 1(a3). In Fig. 1(b3), the singularity distribution is similar to that in Fig. 1(b2), but the intervals of the singularities on the negative x axis become small and those on the positive x axis are enlarged. When $\beta_0 = 7$, the acoustic intensity distribution of the AABV becomes a

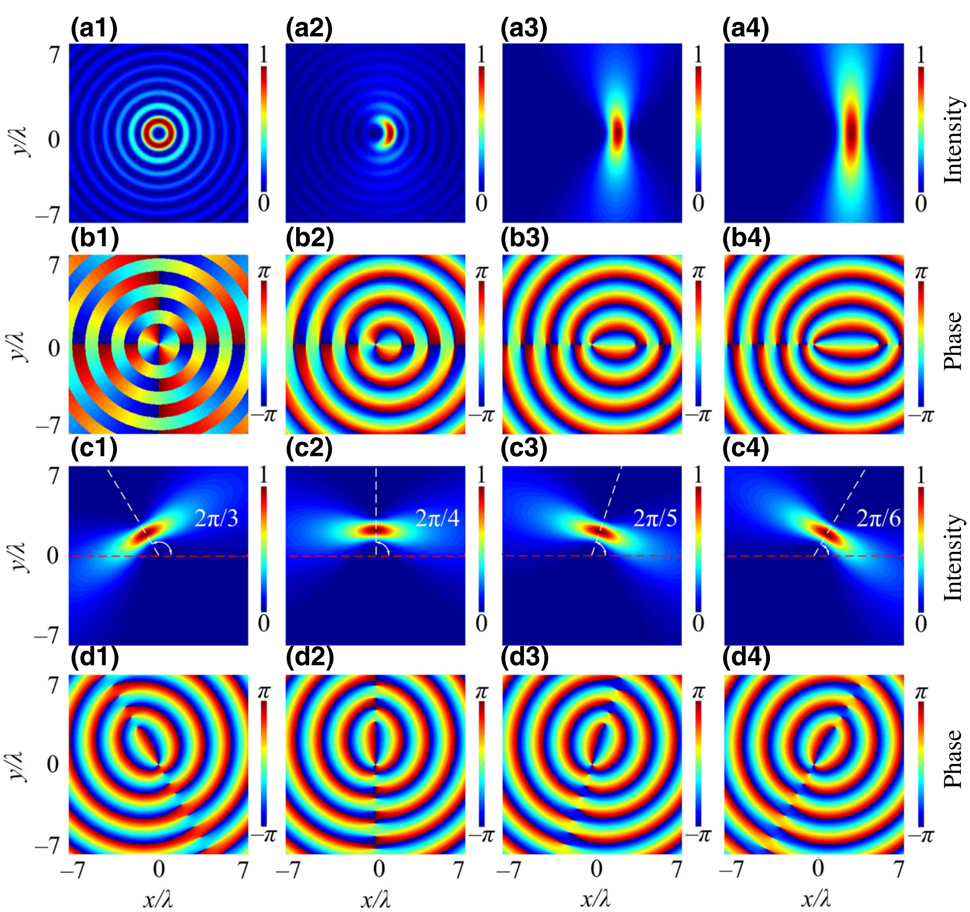

FIG. 1. Normalized theoretical acoustic intensity distributions of the acoustic asymmetric Bessel vortices (AABVs) with (a1) $\beta_0 = 0$, (a2) $\beta_0 = 1$, (a3) $\beta_0 = 4$, and (a4) $\beta_0 = 7$. Here, $\varphi = 0$ and TC $l = 2$. (b1)–(b4) Corresponding phase profiles. Normalized theoretical acoustic intensity distributions of AABVs with (c1) $\varphi = 2\pi/3$, (c2) $\varphi = 2\pi/4$, (c3) $\varphi = 2\pi/5$, and (c4) $\varphi = 2\pi/6$. Here $\beta_0 = 4$ and $l = 2$. (d1)–(d4) Corresponding phase profiles. The observation plane is at $z = 0$.

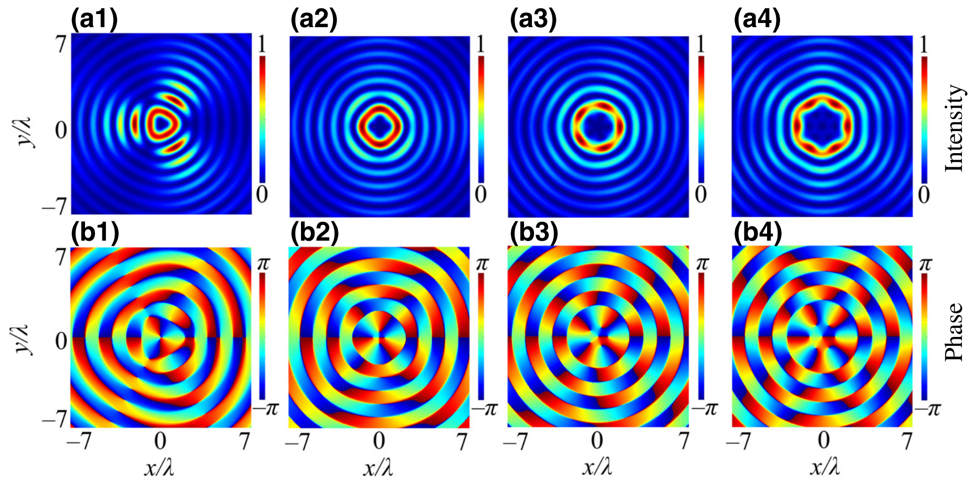

FIG. 2. Normalized theoretical acoustic intensity distributions of the acoustic polygonal Bessel vortices (APBVs) with (a1) $m = 3$, (a2) $m = 4$, (a3) $m = 5$, and (a4) $m = 6$. Here, l and β_0 are fixed at –1 and 4, respectively. (b1)–(b4) Corresponding phase profiles. The observation plane is $z = 0$.

spindle shape, as shown in Fig. 1(a4). It is observed in Fig. 1(b4) that the intervals of the singularities on the negative x axis further decrease and those on positive x axis increase. Therefore, the increase in the asymmetry index leads to continuous increases in the asymmetry of both the acoustic intensity and the phase of the AABV [33,35,36]. Figures 1(c1)–1(c4) show the normalized theoretical acoustic intensity distributions of AABVs with φ of $2\pi/3$, $2\pi/4$, $2\pi/5$, and $2\pi/6$, respectively. Here, $\beta_0 = 4$ and $l = 2$. Figures 1(d1)–1(d4) represent the corresponding phase profiles. It is clearly observed that the φ value almost does not affect the shape of the acoustic intensity and the phase distributions of the AABV, but induces an anticlockwise rotation of the acoustic field with an angle of φ.

Next, we investigate the superimposition of multiple AABVs with different φ. Each AABV has the same parameters except for the φ value that is determined by $\varphi_n = 2\pi(n-1)/m$, $(n = 1, 2, 3 \ldots, m)$, where m is the number of the AABVs. The superposition of m AABVs can be expressed as

$$P_l^m(r,\theta,z) = \sum_{n=1}^{m} p_l(r,\theta,z)|_{\varphi_n}. \tag{3}$$

Figures 2(a1)–2(a4) show the normalized theoretical acoustic intensity distributions based on Eq. (3) for m of 3, 4, 5, and 6, respectively. Here, l and β_0 are fixed at –1 and 4, respectively. The corresponding phase profiles are displayed in Figs. 2(b1)–2(b4). For $m = 3$, the interference of three AABVs with $\varphi_1 = 0$, $\varphi_2 = 2\pi/3$, and $\varphi_3 = 4\pi/3$ forms a triangular ring pattern of acoustic intensity, as shown in Fig. 2(a1). In the phase profile [Fig. 2(b1)], the innermost phase distribution appears as a triangle with a central phase singularity and the phase around this singularity shifts from $-\pi$ to π once in an anticlockwise direction. In addition, three new phase singularities appear very close to the central singularity, which is due to the coupling of three AABVs. In Fig. 2(a2), the superimposition of four AABVs with $\varphi_1 = 0$, $\varphi_2 = 2\pi/4$, $\varphi_3 = 4\pi/4$, and $\varphi_4 = 6\pi/4$ results in a quadrilateral-like ring pattern of acoustic field. A central phase singularity surrounded by four phase singularities can be observed in Fig. 2(b2). As $m = 5$ and $m = 6$, a pentagonlike ring pattern and a hexagonlike ring pattern are observed in Figs. 2(a3) and 2(a4), respectively. Meanwhile, except for the central phase singularity, five and six surrounding phase singularities can be found in Figs. 2(b3) and 2(b4), respectively. Therefore, the superposition of m AABVs with the equal angular spacing of φ can achieve an APBV with m sides. Moreover, with a fixed TC, a larger value of m leads to a higher number of sides and a larger dark central area of the formed polygonal sound field.

Figures 3(a1)–3(a4) show the normalized theoretical acoustic intensity distributions of APBVs with β_0 of 2, 3, 4, and 6, respectively. Here, l and m are fixed at –1 and 4, respectively. The corresponding phase profiles are displayed in Figs. 3(b1)–3(b4). As $\beta_0 = 2$, the interference of four AABVs with $\varphi_1 = 0$, $\varphi_2 = 2\pi/4$, $\varphi_3 = 4\pi/4$, and $\varphi_4 = 6\pi/4$ forms a lattice pattern of acoustic intensity, as shown in Fig. 3(a1). In the phase profile of Fig. 3(b1), the innermost phase around the central phase singularity shifts from $-\pi$ to π, corresponding to the TC $l = -1$. The interference of four AABVs results in four new phase singularities around the central singularity. In Fig. 3(a2), the couplings among four AABVs with $\beta_0 = 3$ produce a cross-shaped acoustic field. In this case, four phase singularities generated by the interference of four AABVs are very close to the central phase singularity [in Fig. 3(b2)]. For $\beta_0 = 4$, a distinct

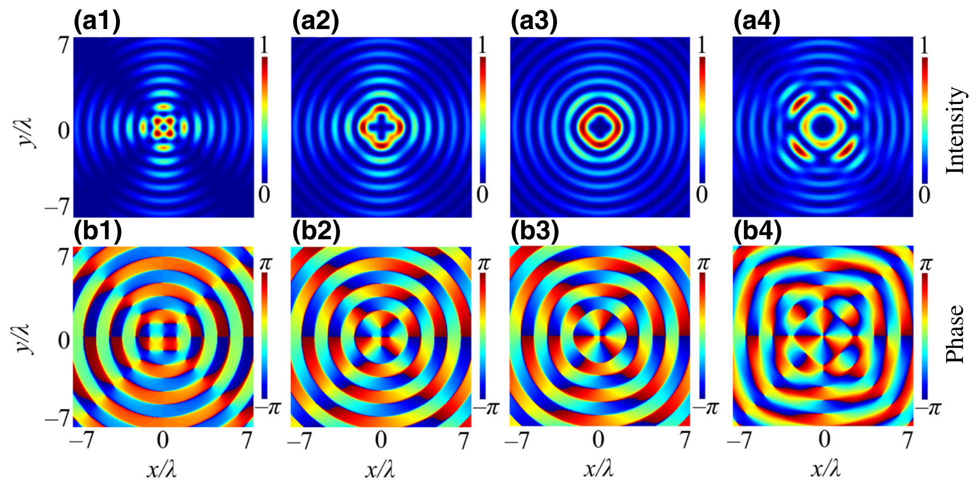

FIG. 3. Normalized theoretical acoustic intensity distributions of the APBVs with (a1) $\beta_0 = 2$, (a2) $\beta_0 = 3$, (a3) $\beta_0 = 4$, and (a4) $\beta_0 = 6$. Here, l and m are fixed at –1 and 4, respectively. (b1)–(b4) Corresponding phase profiles. The observation plane is $z = 0$.

quadrilateral-like ring pattern is observed in the acoustic intensity distribution of Fig. 3(a3). One central phase singularity and four surrounding phase singularities can be found at the central region [in Fig. 3(b3)], leading to the central zero-intensity region. As β_0 further increases to 6, the intensity of the inner quadrilateral-like ring pattern is reduced and those of the peripheral fringes are enhanced, as shown in Fig. 3(a4). This is because the distance of the spindle-shaped acoustic field of the AABV from the coordinate origin increases with increasing β_0 value, and the range of the spindle-shaped acoustic field is also increased. Therefore, the asymmetry index β_0 could adjust the shape of the APBVs.

The influence of the TC of the AABV on the performance of the APBV is further studied. Figures 4(a1)–4(a4) represent the normalized theoretical acoustic intensity distributions of APBVs with l of 1, 2, 3, and 4, respectively. Here, β_0 and m are both fixed at 4. The corresponding phase profiles are shown in Figs. 4(b1)–4(b4). In four cases, the interferences of the AABVs construct a quadrilateral-like ring pattern of the acoustic field and the innermost phase distribution includes a central phase singularity and four surrounding phase singularities. For an APBV whose shape has been determined, with increasing l values, the size of the quadrilateral-like ring pattern of the acoustic field enlarges and the interval between the central phase singularity and the surrounding singularities also increases accordingly. This is mainly because the intensity peak of the AABV expands from the center and grows outwards as the l value increases [33]. In addition, it is surprising in the phase profiles that the phases of all outer rings shift from $-\pi$ to π $(l + 4)$ times in a clockwise direction.

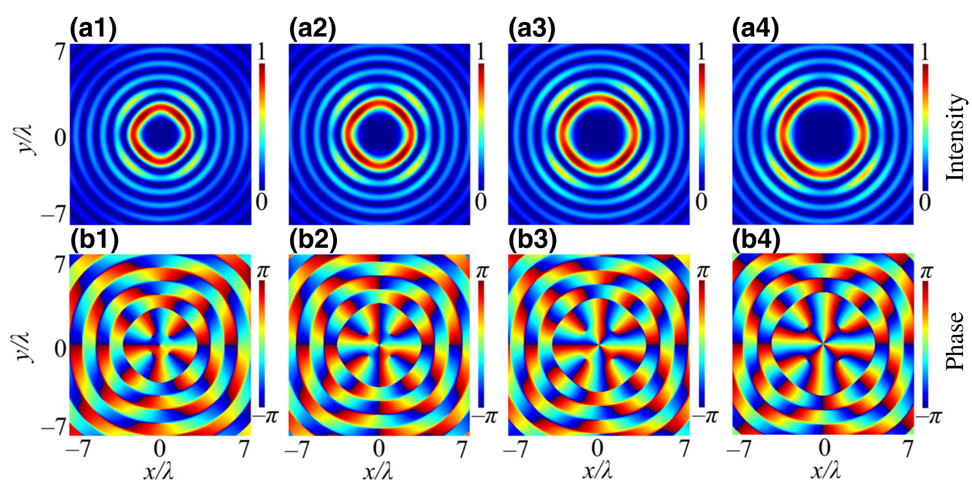

FIG. 4. Normalized theoretical acoustic intensity distributions of the APBVs with (a1) $l = 1$, (a2) $l = 2$, (a3) $l = 3$, and (a4) $l = 4$. Here, β_0 and m are both fixed at 4. (b1)–(b4) Corresponding phase profiles. The observation plane is $z = 0$.

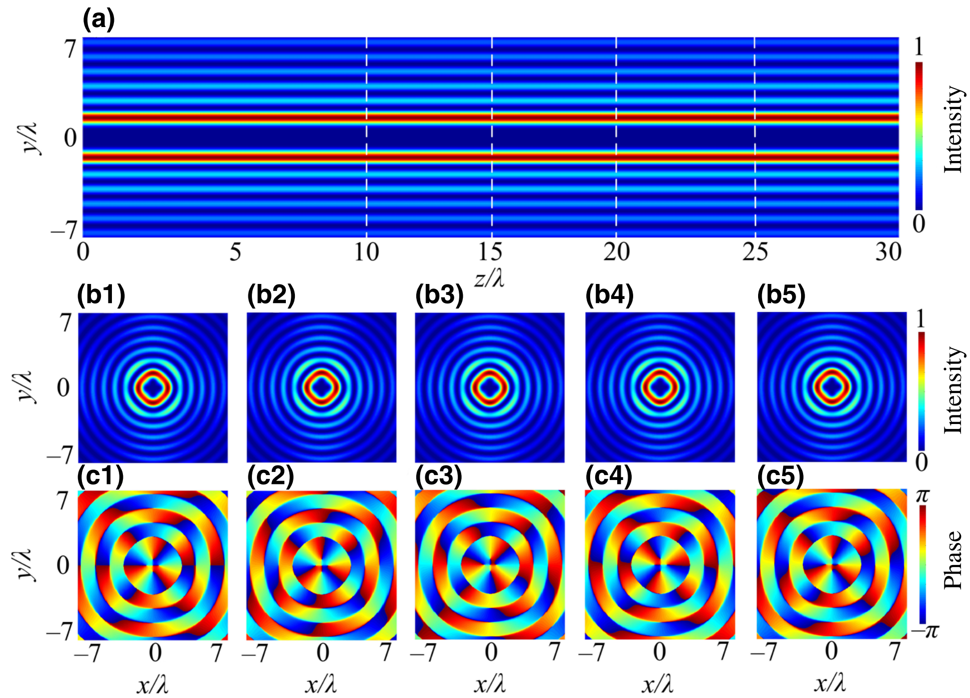

FIG. 5. (a) Normalized theoretical acoustic intensity distribution of the APBV in the y-z plane. Here, l, m, and β_0 are fixed at –1, 4, and 4, respectively. Normalized theoretical acoustic intensity distributions in the cross-sectional planes of (b1) $z = 0$, (b2) $z = 10\lambda$, (b3) $z = 15\lambda$, (b4) $z = 20\lambda$, and (b5) $z = 25\lambda$. (c1)–(c5) Corresponding phase profiles.

We further examine the propagation characteristics of the APBV. Figure 5(a) shows the normalized theoretical acoustic intensity distribution of the APBV in the y-z plane. Here, l, m, and β_0 are fixed at –1, 4, and 4, respectively. It is observed that the APBV could extend to a relatively long distance, and the width between two inner intensity fingers is almost unchanged with increasing z. Figures 5(b1)–5(b5) show the normalized theoretical acoustic intensity distributions of the APBVs in five cross sections of $z = 0$, 10λ, 15λ, 20λ, and 25λ, respectively. The corresponding phase profiles are shown in Figs. 5(c1)–5(c5). The distinct quadrilateral-like ring patterns are observed in all five cross sections. The phase profiles exhibit a rotation with propagation distance because the propagation component of $\exp(ik_r z)$ may undergo an additional phase shift during the propagation process [37,38]. Therefore, the proposed APBV also exhibits excellent nondiffracting characteristics.

III. SIMULATIONS AND EXPERIMENTS

To realize the proposed APBV, an ARM is further designed. Perfectly achieving a vortex requires modulation of both the amplitude and phase of the generator, but it is difficult to control both at the same time [39,40]. Comparing the influences of amplitude and phase on the vortex, we choose a phase-modulated metasurface [39–48]. According to Eq. (3), we extract the required phase distribution of the ARM to generate an APBV with $l = 1$, $\beta_0 = 4$, and $m = 4$, as shown in Fig. 6(a). Here, we set the background medium as air and the working frequency as 15 kHz. The ARM is composed of 110×110 grooved structural units, and the cutaway view of the unit is shown in Fig. 6(b). The unit could be made from a photosensitive resin with a mass density of 1160 kg/m^3 and a sound speed of 2242 m/s, and thus it can be treated as acoustically rigid in air [49,50]. The outer width d of the grooved unit is 5.5 mm, and the outer height w is 11.5 mm. There is a groove inside the unit with a width t of 4.5 mm and a depth of h. The relationship between the reflected phase and amplitude and the groove depth h can be obtained by numerical simulations, as shown in Fig. 6(c). In simulations, the amplitude of incident wave is 1 Pa. It is observed that the depth of the groove mainly affects the reflected phase of the unit but has almost no influence on the reflected amplitude. As the groove depth h changes from 0 to $\lambda/2$, the reflection phase shift of the unit increases from 0 to 2π. Meanwhile, the reflection of the unit can always remain very high (approximately 1). Then, each unit of the ARM is finally designed by comparing the required phase distribution [Fig. 6(a)] with the phase-depth relationship [Fig. 6(c)], and the designed depth distribution of all units of the ARM is shown in Fig. 6(d).

According to the depth distribution in Fig. 6(d), the geometric model of the ARM could be finalized, as shown in Fig. 7(a). Figures 7(b) and 7(c) show the normalized

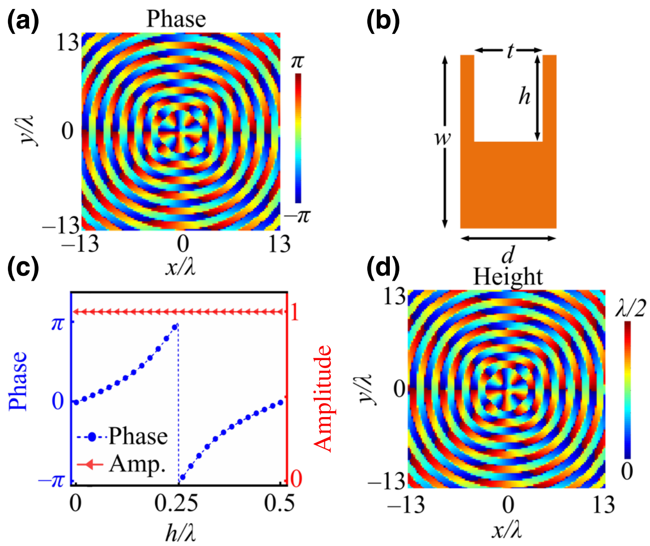

FIG. 6. (a) Required phase distribution of an acoustic reflection metasurface (ARM) to generate an APBV with $l = 1$, $\beta_0 = 4$, and $m = 4$. The background medium is air and the working frequency is 15 kHz. (b) Schematic diagram of the cross section of the grooved unit of the ARM. (c) Variations of reflected amplitude and phase shift of the grooved structural unit with the groove depth h. (d) Depth distribution of the ARM.

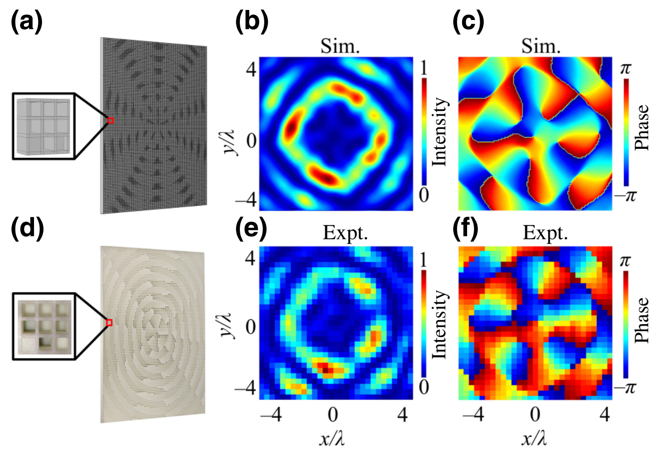

FIG. 7. (a) Three-dimensional configuration of the acoustic reflection metasurface (ARM) for generating the APBV with $l = 1$, $\beta_0 = 4$, and $m = 4$. Normalized simulated (b) acoustic intensity and (c) phase distributions reflected by the ARM. (d) Photograph of the ARM sample. Normalized measured (e) acoustic intensity and (f) phase distributions reflected by the ARM. The observation plane is at $z = 15\lambda$.

simulated acoustic intensity and phase distributions reflected by the ARM. The observation plane is at $z = 15\lambda$. In Fig. 7(b), the acoustic intensity distribution appears as a quadrilateral-like ring pattern. One central phase singularity and four surrounding phase singularities can be found at the central region of the phase profile in Fig. 7(c). These characteristics agree well with the theoretical results shown in Fig. 5. Based on the geometric model shown in Fig. 7(a), we further fabricate an ARM sample via three-dimensional (3D) printing technology, as shown in Fig. 7(d). A loudspeaker with a central frequency of 15 kHz is placed at $z \approx 2$ m ($z \approx 87\lambda$) to produce an incident quasiplane wave. A 1/4-in. microphone (Brüel & Kjær type 4938) is connected with a 3D stepper motor to scan the acoustic fields with a step size of 0.667 cm (approximately 0.3λ) and the distance from the microphone to the ARM sample is fixed at around 15λ. Figures 7(e) and 7(f) show the normalized measured acoustic intensity and phase distributions reflected by the ARM sample. It is observed that the measured acoustic intensity and phase distributions match well with the simulated and analytical results. The few discrepancies are mostly caused by the sample fabrication error, the large measurement step, and the incident quasiplane wave. Therefore, we experimentally demonstrate that the proposed APBV can be achieved by a well-designed ARM.

IV. CONCLUSIONS

We realize an APBV via the coaxial coupling of several AABVs and the number of sides of the APBV is equal to the number of the superimposed AABVs. The influences of the asymmetry coefficient β_0 and TC l of the AABV on the performance of the APBV are investigated. The asymmetry coefficient β_0 can adjust the shape of the APBV and the size of the APBV increases with the l value. We find that the APBV possesses a good nondiffracting feature and can travel over a very large distance. We further construct an ARM with 110×110 grooved units to achieve the APBV in air, as demonstrated by simulations. Ultimately, we fabricate an ARM sample and experimentally confirm that the ARM is capable of producing the APBV. The construction principle of this APBV could also apply to a liquid background medium (see Appendix). The proposed APBV may have more fascinating applications in the manipulation of microparticles and acoustic communication. Compared with a standard vortex, the APBV could be developed for the manipulation of polygonal-shaped particles, collecting microparticles into specific polygonal regions, and translating microparticles along polygonal trajectories. Besides the TC, the complex field of the APBV could provide other carriers, such as the number of sides of the polygonal field, to encode more information, which may increase the channel capacity of APBV-based communication technology.

ACKNOWLEDGMENTS

This work was supported by the National Natural Science Foundation of China (Grants No. 12374439, No.

12174197, No. 12074191, and No. 12027808). X.-R.L. is grateful for the support of China Scholarship Council (Grant No. 202206860015).

APPENDIX: ACOUSTIC POLYGONAL BESSEL VORTEX IN LIQUID

We further demonstrate the theoretical analysis and numerical simulations with a liquid background. Figures 8(a1) and 8(b1) show the theoretical intensity and phase distributions of an acoustic quadrilateral vortex in water, respectively. Here, $l = 1$, $\beta_0 = 4$, $m = 4$, the working frequency is 0.5 MHz, and the observation plane is at $z = 15\lambda$. Comparing Figs. 8(a1) and 8(b1) with Figs. 4(a1) and 4(b1) in the main text, it is found that quadrilateral vortices in both water and liquid exhibit similar field profiles. An ideal plane source composed of 110×110 pixels, with an amplitude of 1 Pa and a phase profile similar to that shown in Fig. 6(a), is further employed to generate the quadrilateral vortex in numerical simulations, and the results are shown in Figs. 8(a2) and 8(b2). The background medium is set as water. The simulations agree well with the theoretical results, proving the possibility of generating an APBV in water. In future experiments, transmitted metasurfaces made of resin or reflected metasurfaces made of stainless steel could be employed to generate an APBV in water. Owing to the orthogonality of the OAM carried by the vortex, the topological charges of the APBV could be used as the information carrier for remote acoustic communication technology. Besides the topological charges, the complex field of the APBV may provide other carriers, such as number of sides of the polygonal field, to encode more information, resulting in a larger channel capacity. This is one application advantage of the polygonal vortex over the doughnut vortex.

In order to demonstrate the application potential on the manipulation of microparticles, we further investigate the Gor'kov potential distribution of a Rayleigh polystyrene (PS) particle in the acoustic quadrilateral vortex field. The Gor'kov potential U can be expressed as follows [51,52]:

$$U = 2\pi r_s^3 \rho_0 \left(\frac{\langle |p|^2 \rangle}{3\rho_0^2 c_0^2} f_1 - \frac{\left\langle \left| \vec{v} \right|^2 \right\rangle}{2} f_2 \right), \tag{A1}$$

Where r_s represents the radius of the particle, p and $\vec{v}$ are the first-order pressure and velocity vector of the acoustic field, and ρ_0 and c_0 are the mass density and sound speed of the background medium. $f_1 = 1 - \kappa'$ and $f_2 = 2(\rho' - 1)/(2\rho' + 1)$ are the contributions of the particle's unipolar and dipolar vibrations, respectively, with $\kappa' = \kappa_p/\kappa_0$ being the compression ratio and $\rho' = \rho_p/\rho_0$ being the density ratio. Here, ρ_p represents the mass density of the particle, κ_0 and κ_p represent the compression moduli of the background medium and the particle, respectively. The PS sphere has a diameter of 300 µm, a mass density of 1050 kg/m^3, a compression modulus of 3.08×10^{-10} 1/Pa, a longitudinal sound speed of 2170 m/s, and a transverse sound speed of 1100 m/s. Then the acoustic radiation force received by the particle in the gradient acoustic field can

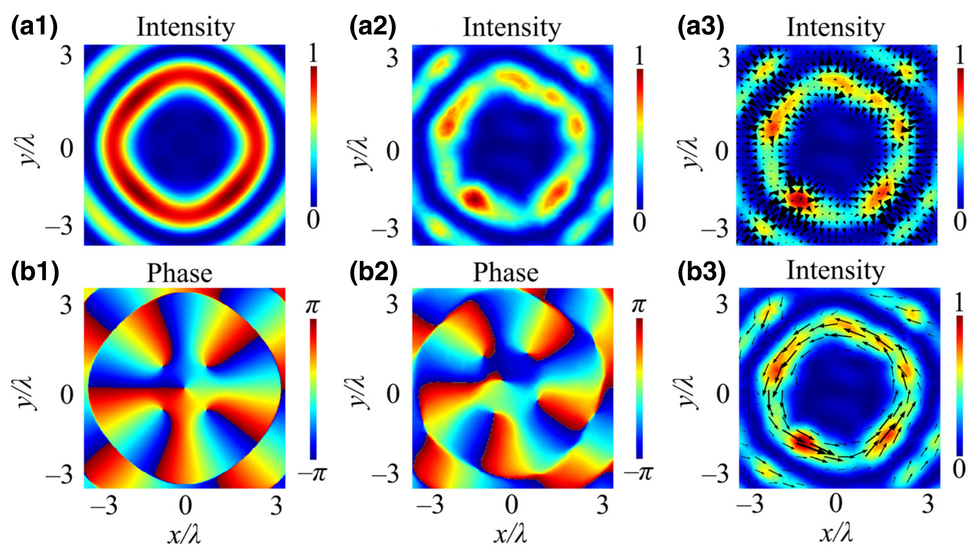

FIG. 8. Acoustic quadrilateral vortices generated in water. Theoretical (a1) intensity and (b1) phase distributions of a quadrilateral vortex. Simulated (a2) intensity and (b2) phase distributions of a quadrilateral vortex generated by an ideal plane source. In both cases, $l = 1$, $\beta_0 = 4$, $m = 4$, the working frequency is 0.5 MHz, and the observation plane is at $z = 15\lambda$. (a3) Acoustic radiation force (black cones) received by a Rayleigh polystyrene particle in the quadrilateral vortex shown in (a2). (b3) Acoustic energy flow density (black arrows) of the quadrilateral vortex shown in (a2).

be calculated as follows [51,52]:

$$F_{\mathrm{rad}} = -\nabla U, \tag{A2}$$

and the calculated results are shown by the black cones in Fig. 8(a3). It is observed that the central quadrilateral forms a quadrilateral potential valley, which indicates that the particle will be pushed into this potential valley. When there are more particles, they could be concentrated into this quadrilateral region. Finally, the acoustic energy flow density $\vec{s} = p\,\vec{v}$ is calculated for this quadrilateral vortex, as shown in Fig. 8(b3). Its annular field presents a trajectory consistent with the quadrilateral acoustic field, and the energy flow is related to the OAM of the vortex, which may play a certain role in the movement of microparticles along the polygonal trajectory. Similar situations could also be found for the cases of other APBVs, such as pentagons and hexagons, which would have characteristics that differ from those of doughnut-shaped acoustic vortices. This is another application advantage of the polygonal vortex over the doughnut vortex, since the latter exhibits a circular intensity field.

[1] Q. X. Zhou, J. Zhang, X. M. Ren, Z. Xu, and X. J. Liu, Acoustic trapping of particles using a Chinese taiji lens, Ultrasonics **110**, 106262 (2021).

[2] Y. C. Luo, Y. R. Jia, J. Yao, D. J. Wu, and X. J. Liu, Enhanced fractional acoustic vortices by an annulus acoustic metasurface with multi-layered rings, Adv. Mater. Technol. **5**, 2000356 (2020).

[3] S. W. Fan, Y. F. Wang, L. Y. Cao, Y. F. Zhu, A. Chen, B. Vincent, B. Assouar, and Y. S. Wang, Acoustic vortices with high-order orbital angular momentum by a continuously tunable metasurface, Appl. Phys. Lett. **116**, 163504 (2020).

[4] X. R. Li, Y. R. Jia, Y. C. Luo, J. Yao, and D. J. Wu, Mixed focused-acoustic-vortices generated by an artificial structure plate engraved with discrete rectangular holes, Appl. Phys. Lett. **118**, 043503 (2021).

[5] Z. Y. Hong, J. Zhang, and B. W. Drinkwater, On the radiation force fields of fractional-order acoustic vortices, Europhys. Lett. **110**, 14002 (2015).

[6] C. Z. Shi, M. Dubois, Y. Wang, and X. Zhang, High-speed acoustic communication by multiplexing orbital angular momentum, Proc. Natl. Acad. Sci. U. S. A. **114**, 7250 (2017).

[7] X. Jiang, B. Liang, J. C. Cheng, and C. W. Qiu, Twisted acoustics: Metasurface-enabled multiplexing and demultiplexing, Adv. Mater. **30**, 1800257 (2018).

[8] W. Q. Wang, S. W. Fan, J. P. Xia, W. Wang, and J. X. Liu, Generation of high-order focused acoustic vortices and multiplexed beams, Appl. Acoust. **214**, 109715 (2023).

[9] Z. Y. Sun, Y. Shi, X. C. Sun, H. Jia, Z. K. Jin, K. Deng, and J. Yang, Underwater acoustic multiplexing communication by pentamode metasurface, J. Phys. D: Appl. Phys. **54**, 205303 (2021).

[10] C. X. Liu, Y. R. Ye, and J. H. Wu, Tunable broadband acoustic vortex generator with multiple orders based on Mie resonances structure, Adv. Mater. Technol. **8**, 2202082 (2023).

[11] X. R. Li, J. J. Feng, B. C. Ping, Y. Sun, D. J. Wu, and B. Assouar, Periodic-phase acoustic vortices with tunable comblike orbital angular momentum spectrum, Phys. Rev. Appl. **20**, 034008 (2023).

[12] T. M. Allen and P. R. Cullis, Drug delivery systems: Entering the mainstream, Science **303**, 1818 (2004).

[13] J. Huang, Q. X. Zhou, X. M. Ren, Z. Xu, and X. J. Liu, Acoustic manipulation on microbubbles along arbitrary trajectories and adjustable destination, Appl. Phys. Lett. **119**, 093503 (2021).

[14] S. H. Tao, W. M. Lee, and X. C. Yuan, Dynamic optical manipulation with a higher-order fractional Bessel beam generated from a spatial light modulator, Opt. Lett. **28**, 1867 (2003).

[15] Y. R. Jia, W. Q. Ji, D. J. Wu, and X. J. Liu, Metasurface-enabled airborne fractional acoustic vortex emitter, Appl. Phys. Lett. **113**, 173502 (2018).

[16] H. Zhang, J. Zeng, X. Y. Lu, Z. Y. Wang, C. L. Zhao, and Y. J. Cai, Review on fractional vortex beam, Nanophotonics **11**, 241 (2022).

[17] H. Ge, Z. W. Long, X. Y. Xu, J. G. Hua, Y. Liu, B. Y. Xie, J. H. Jiang, M. H. Lu, and Y. F. Chen, Direct measurement of acoustic spectral density and fractional topological charge, Phys. Rev. Appl. **19**, 034073 (2023).

[18] J. Durnin, Exact solutions for nondiffraction beams. I. The scalar theory, J. Opt. Soc. Am. A **4**, 651 (1987).

[19] P. Sprangle and B. Hafizi, Comment on nondiffracting beams, Phys. Rev. Lett. **66**, 837 (1991).

[20] L. K. Zhang and P. L. Marston, Optical theorem for acoustic non-diffracting beams and application to radiation force and torque, Biomed. Opt. Express **4**, 1610 (2013).

[21] M. Rajabi and A. Mojahed, Acoustic manipulation: Bessel beams and active carriers, Phys. Rev. E **96**, 043001 (2017).

[22] A. A. Kovalev, V. V. Kotlyar, and A. P. Porfirev, Shifted nondiffractive Bessel beams, Phys. Rev. A **91**, 053840 (2015).

[23] Y. F. Chen, Y. C. Lin, W. Z. Zhuang, H. C. Liang, K. W. Su, and K. F. Huang, Generation of large orbital angular momentum from superposed Bessel beams corresponding to resonant geometric modes, Phys. Rev. A **85**, 043833 (2012).

[24] A. A. Kovalev and V. V. Kotlyar, Orbital angular momentum of superposition of identical shifted vortex beams, J. Opt. Soc. Am. A **32**, 1805 (2015).

[25] G. X. Wang, G. Ji, Z. Y. Li, X. Y. Kang, K. Y. Chen, X. J. Sun, Y. Li, and X. M. Gao, Generation of a polygonal perfect optical vortex array by optical pen, J. Opt. Soc. Am. B **39**, 2506 (2022).

[26] C. Wang, Y. Ren, T. Liu, Z. L. Liu, S. Qiu, Z. M. Li, Y. Ding, and H. Wu, Generating a new type of polygonal perfect optical vortex, Opt. Express **29**, 14126 (2021).

[27] T. Xia, S. B. Cheng, W. X. Yu, W. K. Xie, and S. H. Tao, A polygon-like light-arm zone plate, IEEE Photonics Technol. Lett. **34**, 355 (2022).

[28] Y. G. Zhang, K. B. Yang, P. Li, F. Wen, Y. Z. Gu, and Z. K. Wu, Generation of off-axis phased Gaussian optical array

along arbitrary curvilinear arrangement, Opt. Commun. **527**, 128967 (2023).
[29] Y. J. Shen, Z. S. Wan, Y. Meng, X. Fu, and M. L. Gong, Polygonal vortex beams, IEEE Photonics J. **10**, 1503016 (2018).
[30] Y. Ren, C. Wang, T. Liu, Z. K. Wang, C. Z. Yin, S. Qiu, Z. M. Li, and H. Wu, Polygonal shaping and multi-singularity manipulation of optical vortices via high-order cross-phase, Opt. Express **28**, 26257 (2020).
[31] T. Xia, S. B. Cheng, W. X. Yu, and S. H. Tao, Tailorable polygon-like beams generated by modified spiral petal-like zone plates, Results Phys. **21**, 103823 (2021).
[32] T. Xia, S. B. Cheng, W. X. Yu, and S. H. Tao, A modified multiplexed vortex helico-conical petal-like zone plate, Phys. Scr. **96**, 125529 (2021).
[33] X. Jiang, D. Ta, and W. Q. Wang, Modulation of orbital-angular-momentum symmetry of nondiffractive acoustic vortex beams and realization using a metasurface, Phys. Rev. Appl. **14**, 034014 (2020).
[34] I. S. Gradshteyn and I. M. Ryzhik, *Table of Integrals, Series, and Products* (Academic Press, London, 2014).
[35] V. V. Kotlyar, A. A. Kovalev, and V. A. Soifer, Asymmetric Bessel modes, Opt. Lett. **39**, 2395 (2014).
[36] L. Gong, X. Z. Qiu, Y. X. Ren, H. Q. Zhu, W. W. Liu, J. H. Zhou, M. C. Zhong, X. X. Chu, and Y. M. Li, Observation of the asymmetric Bessel beams with arbitrary orientation using a digital micromirror device, Opt. Express **22**, 26763 (2014).
[37] A. P. Porfirev and R. V. Skidanov, Dark-hollow optical beams with a controllable shape for optical trapping in air, Opt. Express **23**, 8373 (2015).
[38] A. A. Voitiv, J. M. Andersen, M. E. Siemens, and M. T. Lusk, Optical vortex braiding with Bessel beams, Opt. Lett. **45**, 1321 (2020).
[39] B. T. Hefner and P. L. Marston, An acoustical helicoidal wave transducer with applications for the alignment of ultrasonic and underwater systems, J. Acoust. Soc. Am. **106**, 3313 (1999).
[40] X. Jiang, Y. Li, B. Liang, J. Cheng, and L. Zhang, Convert acoustic resonances to orbital angular momentum, Phys. Rev. Lett. **117**, 034301 (2016).
[41] G. Ma, M. Yang, S. Xiao, Z. Yang, and P. Sheng, Acoustic metasurface with hybrid resonances, Nat. Mater. **13**, 873 (2014).
[42] Y. Xie, W. Wang, H. Chen, A. Konneker, B.-I. Popa, and S. A. Cummer, Wavefront modulation and subwavelength diffractive acoustics with an acoustic metasurface, Nat. Commun. **5**, 5553 (2014).
[43] Y. Li, X. Jiang, R. Li, B. Liang, X. Zou, L. Yin, and J. Cheng, Experimental realization of full control of reflected waves with subwavelength acoustic metasurfaces, Phys. Rev. Appl. **2**, 064002 (2014).
[44] Y.-F. Zhu, X.-Y. Zou, R.-Q. Li, X. Jiang, J. Tu, B. Liang, and J.-C. Cheng, Dispersionless manipulation of reflected acoustic wavefront by subwavelength corrugated surface, Sci. Rep. **5**, 1 (2015).
[45] Y. Li, X. Jiang, B. Liang, J. Cheng, and L. Zhang, Metascreen-based acoustic passive phased array, Phys. Rev. Appl. **4**, 024003 (2015).
[46] P. Zhang, T. Li, J. Zhu, X. Zhu, S. Yang, Y. Wang, X. Yin, and X. Zhang, Generation of acoustic self-bending and bottle beams by phase engineering, Nat. Commun. **5**, 4316 (2014).
[47] K. Melde, A. G. Mark, T. Qiu, and P. Fischer, Holograms for acoustics, Nature **537**, 518 (2016).
[48] H. Gao, Z. Gu, B. Liang, X. Zou, J. Yang, J. Yang, and J. Cheng, Acoustic focusing by symmetrical self-bending beams with phase modulations, Appl. Phys. Lett. **108**, 073501 (2016).
[49] W. Q. Ji, Q. Wei, X. F. Zhu, and D. J. Wu, 3D acoustic metasurface carpet cloak based on groove structure units, J. Phys. D: Appl. Phys. **52**, 325302 (2019).
[50] Y. Wang, J. Qian, J. P. Xia, Y. Ge, S. Q. Yuan, H. X. Sun, and X. J. Liu, Acoustic Bessel vortex beam by quasi-three-dimensional reflected metasurfaces, Micromachines **12**, 1388 (2021).
[51] L. P. Gor'kov, On the forces acting on a small particle in an acoustical field in an ideal fluid, Sov. Phys. Dokl. **6**, 773 (1962).
[52] Z. X. Gong and M. Baudoin, Particle assembly with synchronized acoustic tweezers, Phys. Rev. Appl. **12**, 024045 (2019).